Advanced Engineering Materials

ADVANCED ENGINEERING MATERIALS
www.aem-journal.com

RESEARCH ARTICLE OPEN ACCESS

Tailoring Functional Properties of Ti–Ni–Cu Shape Memory Alloy Thin Films for MEMS Actuators

Elaheh Akbarnejad[1] | Aleksander Kostka[2] | Gowtham Arivanandhan[3] | Yujiao Li[2] | Alan Savan[1] | Manfred Kohl[3] | Alfred Ludwig[1]

[1]Materials Discovery and Interfaces, Institute for Materials, Ruhr University Bochum, Bochum, Germany | [2]Center for Interface-Dominated High-Performance Materials (ZGH), Ruhr University Bochum, Bochum, Germany | [3]Institute of Microstructure Technology, Karlsruhe Institute of Technology (KIT), Karlsruhe, Germany

Correspondence: Alfred Ludwig (alfred.ludwig@rub.de)

Received: 8 December 2025 | **Revised:** 4 March 2026 | **Accepted:** 4 March 2026

Keywords: in situ TEM | residual stress | shape memory alloy | thin films | transformation temperatures

ABSTRACT

Ti–Ni–Cu shape memory alloy (SMA) thin films with thicknesses ranging from 150 nm to 1000 nm were deposited by magnetron sputter deposition on planar Si/SiO_2 substrates and prestructured silicon-on-insulator nano-hinges with the aim to provide optimal films for (bidirectional) microelectromechanical systems (MEMS) actuators. SMA films exhibited excellent compositional homogeneity with a minimal deviation of approximately 2 at.% across a 100 mm diameter wafer. The films transitioned from compressive residual stress in the as-deposited state to tensile stress after annealing, with tensile stress values decreasing from 294 to 71 MPa with increasing film thickness. This correlated with a monotonic increase of the transformation temperatures. In situ transmission electron microscopy between room temperature and 100°C confirmed the B19 → B2 phase transformation, consistent with X-ray diffraction results, which also revealed minor B19′ and Ti_2Ni precipitates; atom probe tomography further verified Ti_2Ni formation. An ion beam etching sidewall removal was implemented to eliminate unwanted deposition on nano-hinges, supporting reliable fabrication of bidirectional MEMS actuators.

1 | Introduction

Shape memory alloys (SMAs) show unique properties (high energy density) based on a reversible martensitic transformation, particularly the shape memory effect (SME) and superelasticity, which enable their use in various applications [1]. The development of SMA thin films allows downscaling and miniaturization of actuator systems, for the exploitation of these functional properties at the micro- and nanoscale [2–4]. SME is useful for microelectromechanical systems (MEMS), including in-plane and out-of-plane microactuators, and integrated photonics [5]. Bidirectional microactuators can be used to maintain one of two stable states with minimal energy consumption [6, 7]. The successful implementation of such devices in MEMS is critically dependent on the SMA film's properties, which are influenced by many factors such as composition, phase constitution thickness, lateral dimensions, microstructure, and residual stress. These factors determine the force, stroke, and operational stability of SMA actuators [8].

Binary TiNi SMAs are well known for their robust properties [9]. However, the addition of a third element allows for the tailoring of specific characteristics [10]. Cu addition in particular allows easier synthesis of SMA films as the requirement for stoichiometric films, as it is the case for TiNi, is less strict. Further, Ti–Ni–Cu is known to narrow the thermal transformation hysteresis width and enhance cyclic stability, enabling higher-frequency operation [11, 12]. Since the functional properties of SMA thin films are highly composition-dependent [13], even minor changes can significantly shift transformation temperatures [14]. Ternary Ti–Ni–Cu alloys are less sensitive to composition changes in terms of their martensite transformation temperature and exhibit

a narrower hysteresis range for both temperature and pseudoelasticity. These properties make them more suitable for use as microactuator materials [15].

Sputter deposition under clean high vacuum conditions is a well-controlled method for fabricating thin films [16], with excellent compositional homogeneity across the entire substrate surface. This method is particularly suitable for systems containing Ti, which is prone to oxidation [17, 18]. Post-deposition annealing at elevated temperatures (e.g., 500°C) is necessary to induce crystallinity and obtain the shape memory effect in TiNi-based systems. The resulting residual thermal stress from this fabrication process is a critical parameter, as it impacts transformation behavior, adhesion, film stability, and eventual device performance, e.g., due to unwanted curvature of coated MEMS structures [19].

While considerable progress has been made in understanding the fundamental properties of these materials, a gap remains between fundamental synthesis and materials characterization and successful device integration. This study addresses this gap by providing a holistic view of the critical parameters required to develop well-performing SMA-based MEMS actuators.

Rather than focusing on a single aspect, we bridge materials science and practical device integration by systematically investigating the compositional homogeneity on the wafer level of Ti–Ni–Cu films, characterize and optimize device-relevant film thicknesses specifically chosen for MEMS actuators, and address integration challenges that arise during microfabrication. We correlate film thickness with residual stress evolution, grain growth, phase transformation behavior, and microstructural features such as Ti_2Ni precipitates and interfacial layers.

In particular, we investigate the transformation behavior of Ti–Ni–Cu films in a thickness range matched to out-of-plane and in-plane microactuation requirements, supported by comprehensive compositional energy-dispersive X-ray spectroscopy (EDX) and atom probe tomography (APT) as well as structural analysis using in situ transmission electron microscopy (TEM) and X-ray diffraction (XRD).

In addition, we address a critical but often overlooked challenge in MEMS integration: unwanted SMA sidewall deposition in complex 3D structures. We introduce and validate ion beam etching (IBE) as a scalable solution for sidewall removal in nano-hinges, demonstrating feature sizes comparable to the film thickness. This combined approach connecting thin film optimization directly to a functional fabrication challenge provides a pathway for developing reliable SMA-based microactuators and represents the core contribution of this work.

2 | Materials and Methods

Ti–Ni–Cu thin films of selected thicknesses (150, 300, 600, 800, and 1000 nm) were deposited using an ultrahigh base vacuum magnetron sputter deposition system (DCA Instruments, Finland). A 100 mm diameter $Ti_{54}Ni_{31}Cu_{15}$ alloy target (99.9% purity, FHR) was used to deposit films onto 100 mm diameter Si/SiO_2 wafer substrates at room temperature, i.e., without intentional heating. To evaluate the feasibility of coating microstructured components, prestructured silicon-on-insulator (SOI) nano-hinges were used as substrates [8]. Additionally, Si micro-cantilever stress chips [20] were placed on top of the Si/SiO_2 wafer during deposition to measure residual stress in films deposited under identical conditions. A 30 W RF substrate bias was applied during deposition to moderate the stress in the film. Additionally, a 20 nm Ta adhesion layer was used under the SMA films to improve adhesion, particularly on the SOI substrates.

The base vacuum was 4.8×10^{-6} Pa and depositions were carried out under an Ar (99.9999%) pressure of 0.67 Pa. All depositions were performed in direct current mode, beginning with a 300 target pre-clean at 100 W followed by deposition at 250 W with a deposition rate of 0.42 nm/s.

The as-deposited films were amorphous and required crystallization to exhibit the shape memory effect. Therefore, the films were annealed under instrument control for 2 h at 600°C starting at base vacuum (4.8×10^{-6} Pa) with a heating ramp rate of 50°/min. and natural cooling rate (heater power off), within the sputter chamber. A high-throughput approach was used to investigate the phase transformation properties by temperature-dependent resistivity, R(T), measurements across the wafer. Automated R(T) measurements were performed from −20°C to 120°C with a heating/cooling rate of 5 K/min with 100 mA applied current to determine the phase transformation characteristics. The thin films were further characterized using XRD for phase identification and EDX for composition analysis. EDX point measurements were obtained using a SEM (JEOL JSM-5800) system, with spectra collected for 40 s at a 20 kV acceleration voltage and a 10 mm working distance. XRD measurements were performed using a Bruker D8 Discover diffractometer with Cu Kα radiation ($\lambda = 0.154$ nm). The collected frames were integrated into one-dimensional (1D) diffractograms using DIFFRAC.EVA (Bruker) software.

Residual stress in the films was determined using Si micro-cantilever stress chips by measuring the beam curvature before (R_0) and after (R) deposition. The curvature change is directly proportional to the residual stress in the film and is given by a modified Stoney equation [21]:

$$\sigma_f = \left(\frac{Y_s}{1-\nu_s}\right)\frac{t_s^2}{6t_f}\left(\frac{1}{R}-\frac{1}{R_0}\right) \tag{1}$$

where Y_s is the Young's modulus and ν_s is Poisson's ratio of the cantilever beam material, and t_s and t_f are the thicknesses of the substrate and the film, respectively. The curvature radius and the topography of the cantilever beams were simultaneously captured by a custom-designed digital holographic microscopy (DHM) setup. These stress chips deliver accurate, reproducible stress measurements across a wide thickness range; from nano to micrometers, with a relative error of less than 1%. Image and data analysis methods are detailed in previous work [20, 22].

The 800 nm SMA film was selected for further investigation using high-resolution (scanning) transmission electron microscopy (HR(S)TEM) and APT to gain a near-atomic-scale understanding of phase evolution and composition.

TEM samples were prepared using a FEI Helios G5 CX focused ion beam (FIB) operated at 30 kV. During thinning to the electron transparency, the accelerating voltage of the ion beam was reduced to 16 and then 8 kV. In the final preparation step, low voltage (5 kV) ion-beam cleaning was applied for 2 min on each side of the TEM sample, in order to keep FIB beam damage at a

minimum. A DensSolution Wildfire Nano-Chip GT was used for the in situ TEM heating.TEM analyses were performed using an aberration probe-corrected TEM (JEOL JEM ARM 200F) operated at 200 kV. Electron diffraction analyses were conducted using JEMS software [23] and the following crystal data: B19 icsd: 99364, B2 icsd: 36747, $NiTi_2$ icsd: 646955. Rotational averaging of the spot diffraction patterns was carried out using "DiffTools Diffraction" package [24] in GATAN Digital Micrograph TEM data acquisition software.

APT samples were prepared from the SMA films deposited on flat substrates using the dual-beam FIB system mentioned above, following a standard lift-out method [25]. The APT measurement was performed using voltage mode with 20% pulse fraction on a local electrode atom probe (LEAP 5000 XR, Cameca Instruments) at 65 K at a pulse repetition rate of 200 kHz and a detection rate of 0.005 atoms per pulse. APT data was reconstructed and analyzed by the AP suite 6.3 software.

To reduce SMA film deposition on the sidewalls of the nano-hinges, an IBE process was performed with Ar. The IBE process was conducted using an RIBE Oxford Ionfab300Plus machine. The ion source was operated with an Ar feed (5/10 sccm) at a chamber pressure of 8.3×10^{-3} Pa. The acceleration voltage and current were fixed at 275 V and 190 mA, respectively. The substrate was tilted at −75° relative to the incident beam and rotated at 20 rpm.

3 | Result and Discussion

For the wafer-scale synthesis of SMA MEMS a homogeneous deposition with respect to composition, phase constitution, microstructure, stress, and the reversible phase transformation properties needed to be ensured. Figure S1 and Table S1 show that the compositional variation of the SMA films across the 100 mm diameter wafer in the as-deposited state is below the accuracy limit of EDX (about 1 at.%). No change of composition after annealing is observed.

Figure 1a–e shows results of R(T) measurements in the temperature range of −20°C to 120°C on homogeneous films with thicknesses from 150 to 1000 nm. Thicknesses of the SMA film for the actuator designs needs to be optimized: high film thickness (1000 nm) for actuation would be desirable to achieve large forces and displacements; however, this could conflict with structures of feature size in the range of film thickness, e.g., unwanted sidewall coating on nano-hinges. For too-thin films, the SME could be degraded or even be suppressed; therefore, here we chose a minimal thickness of 150 nm.

Figure 1g shows phase transformation properties determined for all film thicknesses. The red and blue lines of the hysteresis on the graphs show heating and cooling in R(T) measurements respectively. The phase transformation properties are influenced by film thickness: austenite finish (A_f) and martensite start (M_s) temperatures both decrease with decreasing film thickness. A_f drops by ∼26% from 82.8°C at 1000 nm to 61.6°C at 150 nm, and M_s decreases by ∼28% from 76.8°C to 55.1°C over the same thickness range. Figure 1f shows the phase transformation properties across the annealed wafer, at four different coordinates on the wafer. This shows the functional uniformity across the wafer for a homogeneous film with a thickness of 1000 nm. The comparison shows very small deviations in transformation temperatures.

XRD patterns of annealed Ti–Ni–Cu films (600°C, 2 h) measured at room temperature for different thicknesses are shown in Figure 2. XRD patterns were compared with reference patterns from the Inorganic Crystal Structure Database. The films exhibit crystalline structures consisting of a mixture of orthorhombic (B19) and monoclinic (B19′) martensitic phases, along with additional peaks corresponding to the Ti_2Ni phase. The diffraction patterns reveal that for films with lower thickness, the intensity of the diffraction maxima particularly for the (111) plane decrease. B19 martensite is the dominant phase in the 800 nm and 1000 nm thick films. To further investigate the microstructure, TEM and APT analyses were performed on the 800 nm thick film.

A BF-TEM image of the Ti–Ni–Cu film in the as-deposited state (Figure S2) shows a homogeneous, amorphous microstructure. After 2 h of annealing at 600°C, the material has crystallized into two phases of different chemical composition (Figure 3). The TEM analyses show that the Ti-rich phase has formed small, equiaxed grains, uniformly distributed in the volume of the film. Additionally, the area designated x in Figure 3 and Table 1 has the composition of the orthorhombic B19 phase. Furthermore, EDX mapping revealed an approximately 100 nm thick, continuous Ti-rich layer at the interface between the annealed film and the substrate. A 20 nm Ta adhesion layer is present at the substrate interface (blue color in Figure 3e). However, there are overlapping X-ray lines: Ta Mα (1.709 keV) with Si Kα (1.739 keV), and Ta Lα (8.145 keV) with Cu Kα (8.040 keV), which accounts for the abnormally high color intensity and apparent Cu in the Ta layer in Figure 3b,e.

Figure 4 shows two selected area diffraction (SAD) patterns acquired during an in situ TEM heating experiment. Since the combination of the sample and selected area aperture can only confine diffracted beams from a very small number of crystals, a rotational averaging was applied to better visualize the diffracted planes (right inserts of the SAD patterns). The diffracted planes from the room temperature (Figure 4a) orthorhombic (B19) and high temperature (Figure 4b) bcc (B2) phases are highlighted. The volume fraction of the Ti_2Ni phase is lower than the transforming phase and thus its contribution to the SAD pattern is proportionally lower. Moreover, the lattice of the Ti_2Ni phase, is significantly larger ($a_0 = 1.132$ nm ($1.45\ nm^3$)) than B2 phase ($a_0 = 0.306$ nm ($0.0286\ nm^3$)) or B19 phase ($a_0 = 0.291$ nm, $b_0 = 4.288$ nm ($0.0563\ nm^3$)), and thus, its diffracted planes are located inside the strongest ring, close to the transmitted electron beam. Three arrows of Figure 4a highlight planes associated with that phase.

The existence of the Ti_2Ni phase identified by TEM was also confirmed chemically by APT, as shown in Figure 5, where the Ti-rich phase shows 64.35 at.% Ti and 32.74 at.% Ni, close to the stoichiometric composition of Ti_2Ni, while the matrix contains 40.13 at% Ni, 53.20 at% Ti, and 6.36 at% Cu.

The coexistence of B19 and B19′ martensitic phases at room temperature observed in XRD data is consistent with the composition-dependent transformation behavior reported for Ti–Ni–Cu alloys. Systematic studies have demonstrated that the transformation sequence is highly sensitive to Cu content. In particular, Löbel et al. [12]. showed that for $Ti_{51}Ni_{49-x}Cu_x$ thin films, a single-stage B2 → B19′ transformation occurs for Cu contents below 6.5 at.%, while a direct B2 → B19 transformation is

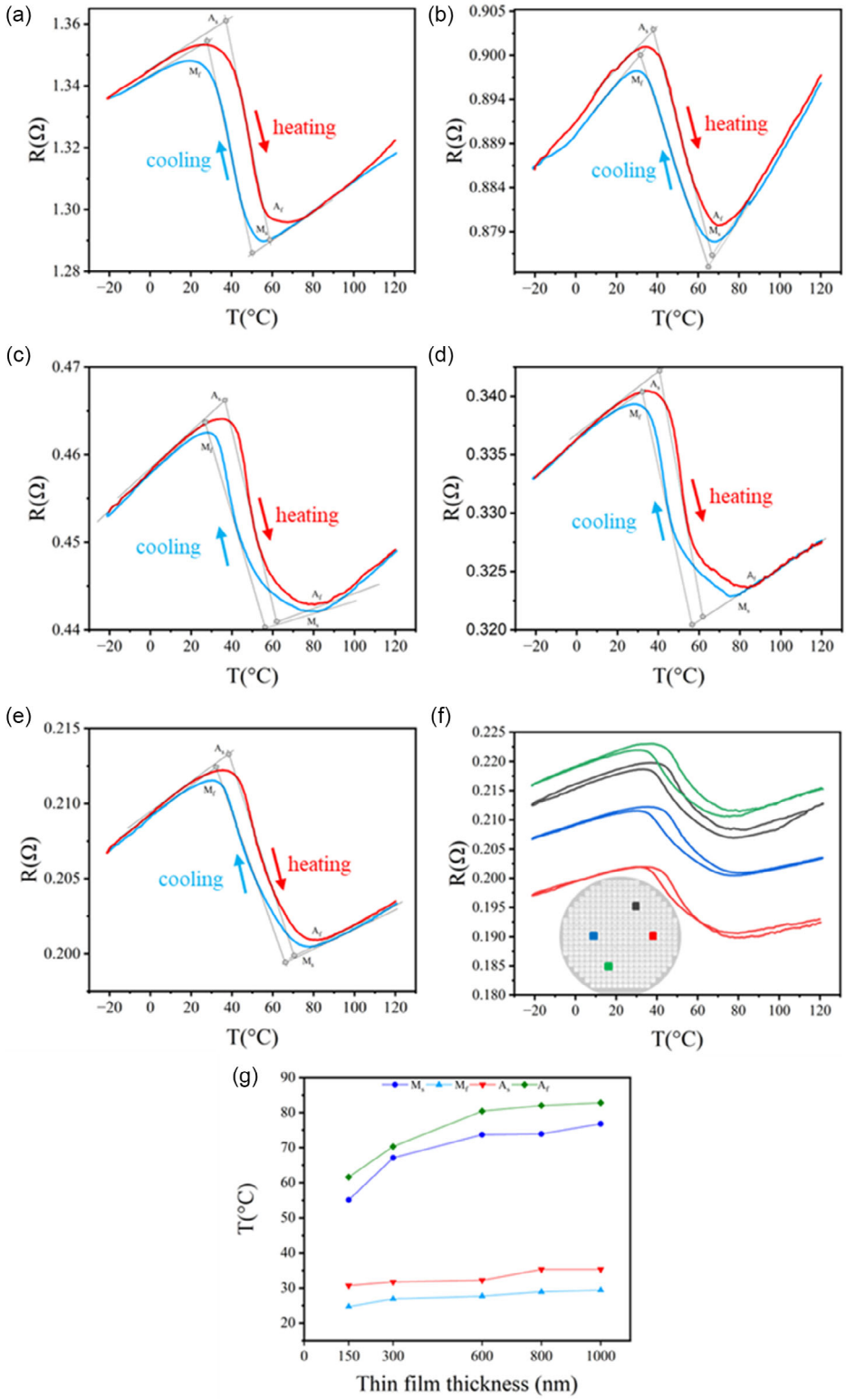

FIGURE 1 | Phase transformation properties of Ti–Ni–Cu SMA thin films determined by R(T) curves showing single-stage transformation after annealing for 2 h at 600°C for film thicknesses of: (a) 150 nm, (b) 300 nm, (c) 600 nm, (d) 800 nm, (e) 1000 nm, (f) measured at four color-coded positions on the wafer level for 1000 nm film thickness; (g) trend of transformation temperatures (M_s, M_f, A_s, A_f) extracted from the R(T) curves in (a–e) in dependence of thin film thickness.

observed above 14 at.% Cu. In the intermediate Cu range, a two-stage B2 → B19 → B19′ transformation takes place. Our APT analysis reveals a matrix Cu content of 6.36 at.%, placing our films near the compositional boundary where both transformation paths are possible. This likely explains the observed mixture of B19 and B19′ phases at room temperature observed in XRD. However, the selected area diffraction patterns in TEM originate from a region approximately 500 nm in

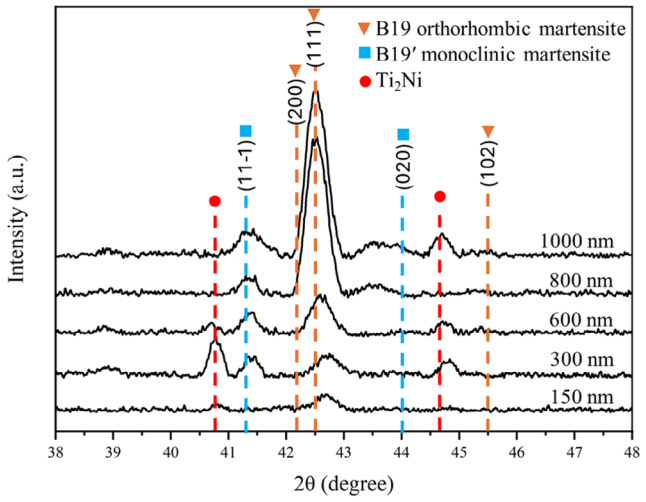

FIGURE 2 | X-ray diffraction patterns of Ti–Ni-–Cu thin films of different film thicknesses measured at room temperature after annealing for 2 h at 600°C.

TABLE 1 | TEM-EDX quantitative analysis of two distinctive regions highlighted in Figure 3. The data represent averaged (measured in several regions), not standardized, normalized elemental composition in at.%. C and Ga were excluded from the quantification as artefacts from FIB sample preparation.

Data	Ti, at.%	Ni, at.%	Cu, at.%
X	45.1	39.3	15.6
Y	58.6	34.9	5.5
Z	61.8	32.4	5.2

diameter, which samples a relatively small number of crystallites. We could not clearly resolve the B19′ phase in the TEM data. Therefore, the apparent discrepancy between the XRD and TEM techniques is attributed to the statistical limitations of TEM rather than the absence of the B19′ phase.

The presence of Ti_2Ni precipitates, identified in this work by XRD, TEM, and APT, can influence the martensitic

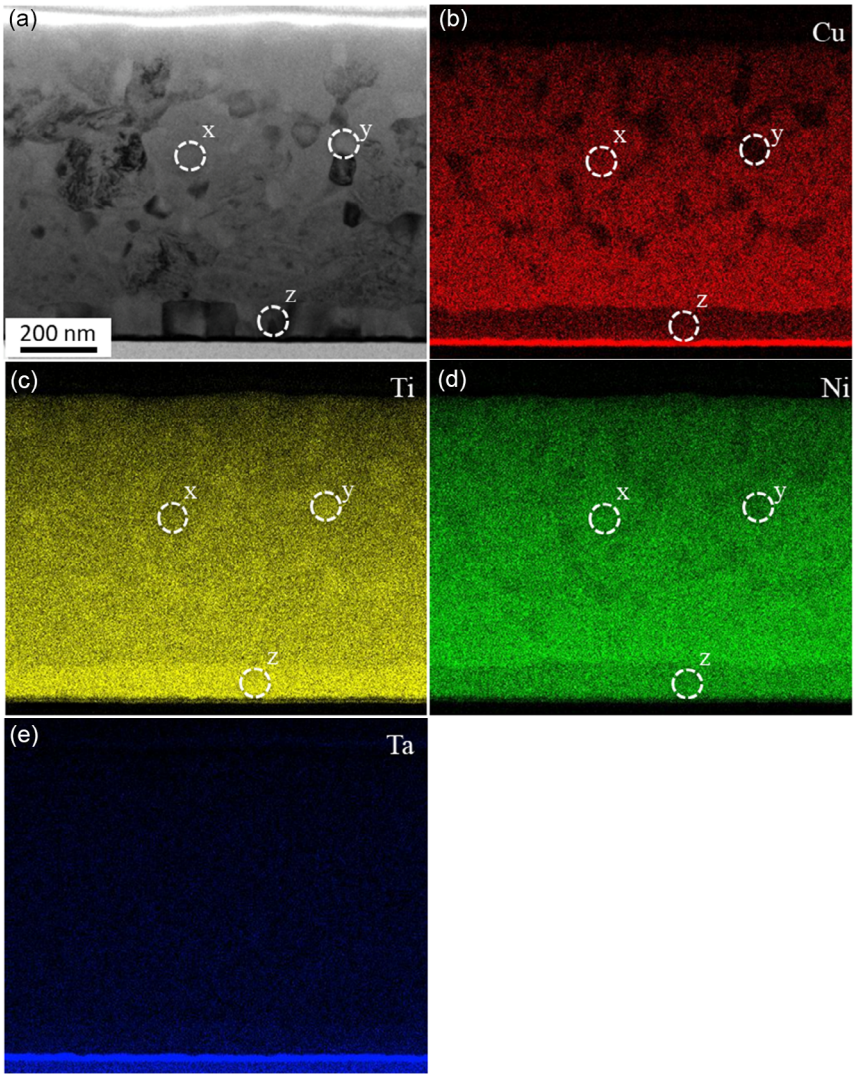

FIGURE 3 | TEM analyses of the annealed (800 nm, 600°C, 2 h) Ti–Ni–Cu SMA. (a) BF TEM image, and (b)–(e) corresponding EDX elemental maps for Cu, Ti, Ni, and Ta, respectively. Several regions (indicated as *x*, *y*, and *z*) were selected for quantitative analysis, with the results provided in Table 1.

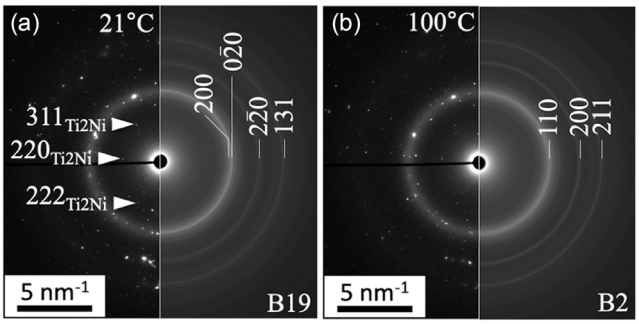

FIGURE 4 | Results of in-situ TEM heating experiments showing the phase transformation from the (a) room temperature B19 phase to the (b) high temperature B2 phase. Diffracted planes corresponding to the Ti_2Ni phase are indicated on both patterns.

transformation by acting as obstacles that impede the formation and movement of phase boundaries, thereby affecting transformation temperatures [26]. Additionally, studies have shown that Ti_2Ni precipitates can hinder dislocation motion and micro-crack propagation, contributing to a hardening effect linked to improved cyclic stability in fine-grained microstructures [27]. Regarding hysteresis width, Zarnetta et al. reported that Ti_2Ni(Pd) precipitates were responsible for the linear increase of thermal hysteresis with increasing Ti content [28]. In the present work on Ti–Ni–Cu films, we observed no clear trend in hysteresis width with film thickness, suggesting that hysteresis is primarily governed by the Cu content rather than by the presence of Ti_2Ni precipitates.

Concerning the driving factors for Ti_2Ni formation, we attribute their presence to the combined effects of annealing conditions and interfacial phenomena. The Ti-rich layer observed near the substrate interface suggests that interfacial diffusion plays a role in local composition variations, which may promote precipitation. Film thickness also appears to influence the distribution and density of these precipitates, likely due to differences in grain size and diffusion paths.

The interfacial layers at the substrate–film interface and the surface are inevitable. Both the presence of Ti_2Ni precipitates and the Ti-rich interfacial layer (~100 nm) near the substrate influence the effective composition of the surrounding matrix. Since Ti is consumed at these reactive interfaces and within precipitates, the remaining SMA matrix becomes relatively Ti-depleted. This local compositional shift can alter the martensitic transformation temperatures, as the transformation behavior in Ti–Ni–Cu alloys is highly composition-sensitive. Therefore, optimizing the film properties requires careful consideration of the starting composition, processing conditions, and their combined effect on the resulting phase transformation characteristics.

The functionality of MEMS depends also on the residual stresses of the films they are composed of. Figure 6 shows the residual stresses of the investigated SMA films. The films show a transition from compressive stress in the as-deposited condition (−331, −236, −119, −87, and −130 MPa for 150, 300, 600, 800, and

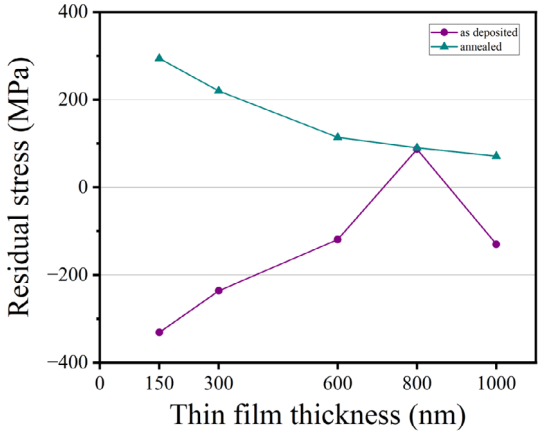

FIGURE 6 | Trend lines for residual stress in dependence of film thickness, based on the measurement results in Table S2. The graph shows the transition from compressive stress in the as-deposited state to tensile stress after annealing for 2 h at 600°C.

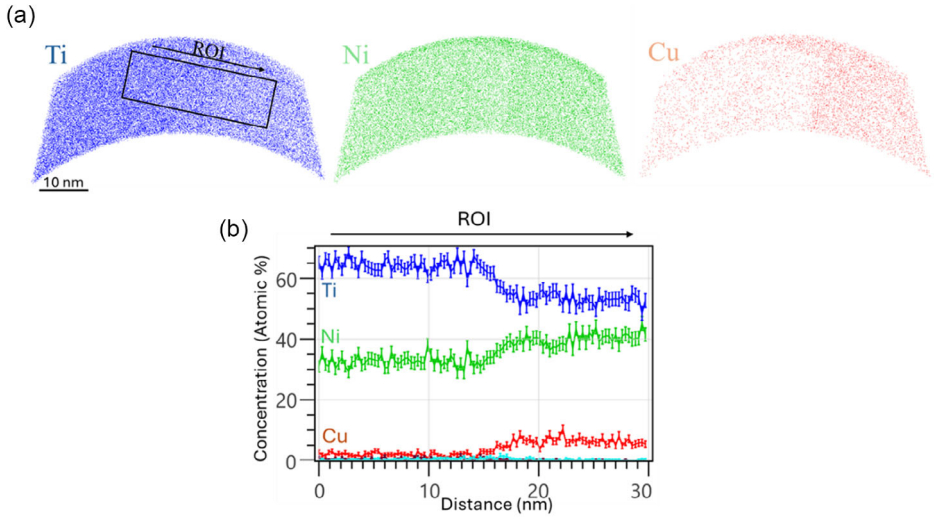

FIGURE 5 | Results of APT investigation of a Ti–Ni–Cu SMA tip: (a) Elemental distributions of Ti (blue), Ni (green), Cu (red), within a 5 nm-thick slice in the side views of the APT tip. The region of interest (ROI) (30 x 10 x 5 nm^3), indicated by the black box, was chosen for the 1D composition profiles. The arrow indicates the direction along which the composition profiles are plotted. (b) 1D composition profile for the selected ROI indicated in (a).

1000 nm, respectively) to tensile stress after annealing at 600°C for 2 h (294, 220, 114, 90, and 71 MPa for the same thicknesses).

The transformation temperatures increase monotonically with film thickness and correlate with the reduction in residual tensile stress. At first glance, this seems to contradict the expected Clausius–Clapeyron behavior for constrained SMA films, where lowering tensile stress should decrease transformation temperatures [29]. This apparent discrepancy requires closer examination of the underlying mechanisms.

In thin films, strong substrate clamping produces large biaxial tensile stresses that partially oppose the martensitic transformation. However, stress is not an independent variable during annealing, it evolves together with the microstructure. For films with increasing thickness, the substrate constraint weakens and the grain structure coarsens. The dominant mechanism governing the transformation temperature trend is this thickness-dependent grain growth.

Studies on nanocrystalline NiTi alloys show that transformation temperatures decrease with decreasing grain size because grain boundaries constrain martensite nucleation [30]. The thinnest films (150 nm) therefore have the smallest grains, the strongest constraint, and the lowest transformation temperatures. As thickness increases to 300, 600, 800, and 1000 nm, grain growth reduces this constraint, allowing transformation at progressively higher temperatures.

The accompanying reduction in tensile stress should be viewed as a parallel consequence of grain coarsening; grain growth is a known stress-relaxation mechanism in thin films [31] rather than an independent driving factor for the temperature shift. While changes in stress may contribute to Clausius–Clapeyron, their influence is secondary to the dominant grain-size effect.

Recognizing grain size as the primary mechanism, and stress relaxation as a correlated outcome, explains the smooth, monotonic increase in transformation temperatures from 150 nm to 1000 nm and resolves the apparent contradiction with Clausius–Clapeyron predictions. This interpretation also aligns with the thickness-dependent behavior reported by König et al. [32]. for Ti–Ni–Cu films, particularly in the 150–400 nm range.

Furthermore, lateral structuring of SMA films can significantly influence their transformation behavior, particularly when the structural width is reduced. Oellers et al. [33]. reported that for patterned $Ti_{48}Ni_{40}Cu_{12}$ films with lateral widths decreasing from 1960 nm to 1060 nm, the transformation temperatures showed a slight increase. This trend continued with further lateral width reduction from 1060 to 750 nm, indicating weakening driving force for phase transformation. The behavior observed in the range of 1060 to 750 nm is comparable to our results, although the absolute transformation temperatures differ. For our 1000 nm SMA film, we measured an A_f of 82.8°C and a M_s of 76.8°C. In contrast, Oellers et al. report 37°C for A_f and 40°C for M_s for their 1060 nm patterned film. These differences can be attributed to different geometries. Additionally, Kohl et al. [4]. demonstrated that the SME persists in freestanding Ni-Mn-Ga double-beam nanoactuators with beam widths down to 100 nm and thicknesses of 125 nm. However, they observed reduced electrical resistance changes and increased dominance of surface energy effects at this scale. This indicates the presence of size effects with lateral dimensions below 200 nm.

The shift in transformation temperatures can also be explained by composition changes arising from surface-related effects. In wafer-level TiNi-based films, mainly the top surface oxidizes, typically forming a ~20–30 nm Ti_xO_x layer, which locally changes the composition and can create Ni-rich regions beneath the oxide [32]. To achieve structures with feature sizes comparable to the film thickness, the SMA layer was integrated into prestructured Si [34]. In nano-hinge geometries, however, deposition of SMA along the sidewall is unavoidable, and oxidation occurs not only on the top surface but also along these deposited sidewalls. This additional sidewall material introduces compositional variations that may further affect the transformation temperatures of the SMA. Wet chemical etching, typically using HF-HNO_3 solutions, can be used to remove this sidewall coating; however, this process is inherently isotropic and leads to large lateral undercut, which makes it unsuitable for achieving sub-micron features [35, 36]. FIB milling enables geometrically precise sub-micron features but is intrinsically a low-throughput technique and therefore not compatible for scalable manufacturing [37, 38].

Alternatively, IBE can be used to remove the undesired SMA deposited along the nano-hinge sidewalls. To study the effectiveness of this approach, nano-hinges were fabricated using SOI technology with designed hinge widths of 0.3, 0.4, and 0.5 µm. Figure 7a shows the result of the deposition of a 600 nm thick

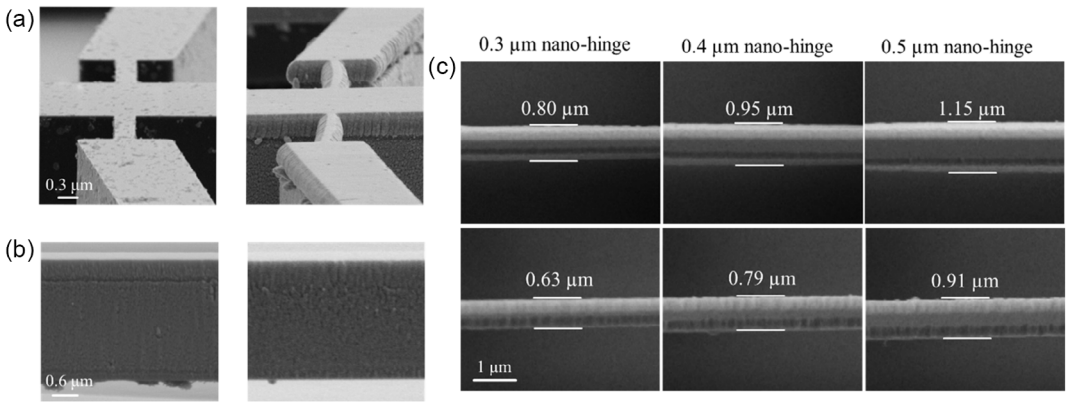

FIGURE 7 | Results of the deposition of the Ti–Ni–Cu film and sidewall removal using the IBE process. The SEM images of (a) pre-structured Si nano-hinges before and after Ti–Ni–Cu deposition, (b) side view of the nano-hinge before and after the IBE process, and (c) top view comparison of nano-hinges before and after the IBE process for Si hinge widths of 0.3, 0.4, and 0.5 µm.

Ti–Ni–Cu film on Si nano-hinges. An IBE process was performed with substrate tilted at −75° relative to the incident beam in order to predominantly target etch the nano-hinge sidewalls. Figure 7b compares the coated nano-hinges before and after the IBE process, confirming that the top surface film thickness is largely maintained. Figure 7c shows Ti–Ni–Cu deposition on Si nano-hinges with designed beam widths of 0.3, 0.4, 0.5 µm. Following the 600 nm Ti–Ni–Cu deposition, approximately 250–300 nm of material is deposited on each sidewall of the nano-hinges. After 10 min of IBE processing, about 80–120 nm of the sidewall film is removed from each side. Further etching would risk excessive removal of the top surface, thereby affecting the transformation properties.

4 | Conclusion

Ti–Ni–Cu SMA thin films with thicknesses between 150 and 1000 nm were deposited and optimized for their integration into MEMS actuators. Annealing at 600°C for 2 h produced crystalline films exhibiting clear martensitic and austenitic transformations, with all transformation temperatures increasing with film thickness. Stress characterization was realized using Si microcantilever stress chips measured by DHM: the residual stress changes from compressive to tensile after annealing and the tensile stress values decrease with increasing film thickness. Sidewall deposition, which is limiting nano-hinge mobility and bidirectional actuation, was effectively reduced using an IBE process. The ability to remove and control SMA sidewall coverage establishes an advance beyond existing thin film studies and a contribution to reliable microactuator fabrication. Detailed structural characterization of the 800 nm film using XRD and in situ TEM heating, revealed B19 martensite and B2 austenite. The presence of Ti_2Ni precipitates was identified by both APT and TEM, consistent with XRD peaks, and TEM-EDX mapping further showed that the Ti-rich phase has formed of a ∼100 nm interfacial layer close to the substrate along with the small, equiaxed grains, uniformly distributed in the volume of the film. These results demonstrate that the thickness of Ti–Ni–Cu films can be tailored to provide reliable transformation behavior, controlled stress states, and controlled microfabrication interfaces. This forms a robust platform for the development of future SMA-based MEMS microactuators.

Author Contributions

Elaheh Akbarnejad: conceptualization: (lead), data curation: (lead), formal analysis: (lead), investigation: (lead), methodology: (lead), validation: (lead), visualization: (lead), writing – original draft: (lead), writing – review & editing: (lead). **Aleksander Kostka:** data curation: (supporting), investigation: (equal), methodology: (supporting), visualization: (equal), writing – review & editing: (supporting). **Gowtham Arivanandhan:** investigation: (supporting), methodology: (supporting), visualization: (supporting), writing – review & editing: (supporting). **Yujiao Li:** investigation: (equal), methodology: (supporting), writing – review & editing: (supporting). **Alan Savan:** methodology: (supporting), writing – review & editing: (supporting). **Manfred Kohl:** conceptualization: (lead), funding acquisition: (lead), methodology: (equal), resources: (lead), supervision: (equal), writing – review & editing: (supporting). **Alfred Ludwig:** conceptualization: (lead), funding acquisition: (lead), methodology: (lead), project administration: (lead), resources: (lead), supervision: (lead), writing – original draft: (supporting), writing – review & editing: (lead).

Acknowledgments

The authors acknowledge the financial support by the German Science Foundation (DFG) within the Priority Program "SPP2206 - Cooperative Multilevel Multistable Microactuator Systems." The ZGH at Ruhr University Bochum is acknowledged for use of its facilities. This work was partly carried out with the support of the Karlsruhe Nano Micro Facility (KNMFi, www.knmf.kit.edu), a Helmholtz Research Infrastructure at Karlsruhe Institute of Technology (KIT, www.kit.edu).

Open Access funding enabled and organized by Projekt DEAL.

Funding

This study was supported by Deutsche Forschungsgemeinschaft.

Conflicts of Interest

The authors declare no conflicts of interest.

Data Availability Statement

Data openly available in a public repository that does not issue DOIs. https://mdi.matinf.pro/object/shape_memory_alloy.

References

1. Y. Fu and H. Du, "RF Magnetron Sputtered TiNiCu Shape Memory Alloy Thin Film," *Materials Science and Engineering: A* 339 (2003): 10–16, https://doi.org/10.1016/S0921-5093(02)00130-2.

2. J. F. Gómez-Cortés, M. L. Nó, A. Chuvilin, I. Ruiz-Larrea, and J. M. S. Juan, "Thermal Stability of Cu-Al-Ni Shape Memory Alloy Thin Films Obtained by Nanometer Multilayer Deposition," *Nanomaterials (Basel, Switzerland)* 13 (2023), https://doi.org/10.3390/nano13182605.

3. S. Shiva, N. Yadaiah, I. A. Palani, C. P. Paul, and K. S. Bindra, "Thermo Mechanical Analyses and Characterizations of TiNiCu Shape Memory Alloy Structures Developed by Laser Additive Manufacturing," *Journal of Manufacturing Processes* 48 (2019): 98–109, https://doi.org/10.1016/j.jmapro.2019.11.003.

4. M. Kohl, M. Schmitt, A. Backen, L. Schultz, B. Krevet, and S. Fähler, "Ni-Mn-Ga Shape Memory Nanoactuation," *Applied Physics Letters* 104 (2014), https://doi.org/10.1063/1.4863667.

5. K. Chaudhary, V. K. Haribhakta, and P. V. Jadhav, "A Review of Shape Memory Alloys in MEMS Devices and Biomedical Applications," *Materials Today: Proceedings* (2024), https://doi.org/10.1016/j.matpr.2024.04.105.

6. P. Krulevitch, A. P. Lee, P. B. Ramsey, J. C. Trevino, J. Hamilton, and M. A. Northrup, "Thin film shape memory alloy microactuators," *Journal of Microelectromechanical Systems* 5 (1996): 270–282, https://doi.org/10.1109/84.546407.

7. R. Vitushinsky, S. Schmitz, and A. Ludwig, "Bistable Thin-Film Shape Memory Actuators for Applications in Tactile Displays," *Journal of Microelectromechanical Systems* 18 (2009): 186–194, https://doi.org/10.1109/JMEMS.2008.2009816.

8. G. Arivanandhan, E. Akbarnejad, A. Ludwig, and M. Kohl, in *2025 23rd International Conference on Solid-State Sensors, Actuators and Microsystems (Transducers)* (IEEE, 2025), 829–832.

9. D. Piorunek, J. Frenzel, N. Jöns, C. Somsen, and G. Eggeler, "Chemical Complexity, Microstructure and Martensitic Transformation in High Entropy Shape Memory Alloys," *Intermetallics* 122 (2020), https://doi.org/10.1016/j.intermet.2020.106792.

10. W. J. Moberly, J. L. Proft, T. W. Duerig, and R. Sinclair, "Twinless Martensite in TiNiCu Shape Memory Alloys," *Materials Science Forum* 56-58 (1990): 605–610, https://doi.org/10.4028/www.scientific.net/MSF.56-58.605.

11. R. Zarnetta, P. J. S. Buenconsejo, A. Savan, S. Thienhaus, and A. Ludwig, "High-Throughput Study of Martensitic Transformations in the Complete Ti–Ni–Cu System," *Intermetallics* 26 (2012): 98–109, https://doi.org/10.1016/j.intermet.2012.03.044.

12. R. Löbel, S. Thienhaus, A. Savan, and A. Ludwig, "Combinatorial Fabrication and High-Throughput Characterization of a Ti–Ni–Cu Shape Memory Thin Film Composition Spread," *Materials Science and Engineering: A* 481-482 (2008): 151–155, https://doi.org/10.1016/j.msea.2007.02.168.

13. Y. Yamabe-Mitarai, T. Hara, T. Kitashima, S. Miura, and H. Hosoda, "Composition Dependence of Phase Transformation Behavior and Shape Memory Effect of Ti, Pt, Ir," *Journal of Alloys and Compounds* 577 (2013): S399–S403, https://doi.org/10.1016/j.jallcom.2012.02.136.

14. R. Zarnetta, M. Ehmann, A. Savan, and A. Ludwig, "Identification of Optimized Ti–Ni–Cu Shape Memory Alloy Compositions for High-Frequency Thin Film Microactuator Applications," *Smart Materials and Structures* 19 (2010), https://doi.org/10.1088/0964-1726/19/6/065032.

15. A. Ishida and S. Miyazaki, "Microstructure and Mechanical Properties of Sputter-Deposited Ti-Ni Alloy Thin Films," *Journal of Engineering Materials and Technology* 121 (1999): 2–8, https://doi.org/10.1115/1.2815996.

16. A. Ishida, M. Sato, and Z. Y. Gao, "Properties and Applications of TiNiCu Shape-Memory-Alloy Thin Films," *Journal of Alloys and Compounds* 577 (2013): S184–S189, https://doi.org/10.1016/j.jallcom.2011.12.155.

17. S. K. Sharma, S. Mohan, S. Bysakh, A. Kumar, and S. V. Kamat, "Nanoscale Compositional Analysis of NiTi Shape Memory Alloy Films Deposited by DC Magnetron Sputtering," *Journal of Vacuum Science and Technology A: Vacuum, Surfaces, and Films* 31 (2013), https://doi.org/10.1116/1.4816841.

18. H. Kato, J. Hino, K. Sasaki, and S. Inoue, "Sputtering Growth of Ni–Ti Shape Memory Alloy Nano Fibers on Porous Alumina Membrane," *Journal of Alloys and Compounds* 577 (2013): S222–S226, https://doi.org/10.1016/j.jallcom.2012.02.042.

19. Y. Q. Fu, S. Sanjabi, Z. H. Barber, et al., "Evolution of Surface Morphology in TiNiCu Shape Memory Thin Films," *Applied Physics Letters* 89 (2006), https://doi.org/10.1063/1.2361275.

20. D. Grochla, L. Banko, J. Pfetzing-Micklich, H. Behm, R. Dahlmann, and A. Ludwig, "Si Micro-Cantilever Sensor Chips for Space-Resolved Stress Measurements in Physical and Plasma-Enhanced Chemical Vapour Deposition," *Sensors and Actuators A: Physical* 270 (2018): 271–277, https://doi.org/10.1016/j.sna.2017.12.050.

21. G. G. Stoney, "The Tension of Metallic Films Deposited by Electrolysis," *Proceedings of the Royal Society of London. Series A* 82 (1909): 172–175, https://doi.org/10.1098/rspa.1909.0021.

22. Y. W. Lai, S. Hamann, M. Ehmann, and A. Ludwig, "High-Throughput Characterization of Stresses in Thin Film Materials Libraries Using Si Cantilever Array Wafers and Digital Holographic Microscopy," *Review of Scientific Instruments* 82 (2011), https://doi.org/10.1063/1.3600594.

23. P. Stadelmann, *Electron Microscopy Software Java* (JEMS-SWISS, 1999).

24. D. R. G. Mitchell, "DiffTools: Electron Diffraction Software Tools for DigitalMicrograph," *Microscopy Research and Technique* 71 (2008): 588–593, https://doi.org/10.1002/jemt.20591.

25. K. Thompson, D. Lawrence, D. J. Larson, J. D. Olson, T. F. Kelly, and B. Gorman, "In Situ Site-Specific Specimen Preparation for Atom Probe Tomography," *Ultramicroscopy* 107 (2007): 131–139, https://doi.org/10.1016/j.ultramic.2006.06.008.

26. J. X. Zhang, M. Sato, and A. Ishida, "On the Ti2Ni Precipitates and Guinier–Preston Zones in Ti-Rich Ti–Ni Thin Films," *Acta Materialia* 51 (2003): 3121–3130, https://doi.org/10.1016/S1359-6454(03)00124-1.

27. H. Z. Lu, L. H. Liu, C. Yang, et al., "Simultaneous Enhancement of Mechanical and Shape Memory Properties by Heat-Treatment Homogenization of Ti_2Ni Precipitates in TiNi Shape Memory Alloy Fabricated by Selective Laser Melting," *Journal of Materials Science & Technology* 101 (2022): 205–216, https://doi.org/10.1016/j.jmst.2021.06.019.

28. R. Zarnetta, E. Zelaya, G. Eggeler, and A. Ludwig, "Influence of Precipitates on the Thermal Hysteresis of Ti–Ni–Pd Shape Memory Thin Films," *Scripta Materialia* 60 (2009): 352–355, https://doi.org/10.1016/j.scriptamat.2008.11.001.

29. Y. Liu and H. Yang, "The Concern of Elasticity in Stress-Induced Martensitic Transformation in NiTi," *Materials Science and Engineering: A* 260 (1999): 240–245, https://doi.org/10.1016/S0921-5093(98)00959-9.

30. Z. Zhao, J. Lin, Y. Xiao, and J. Min, "Effects of Grain Size and Dislocation Density on Thermally-Induced Martensitic Transformation of Nanocrystalline NiTi Alloys," *Journal of Alloys and Compounds* 978 (2024), https://doi.org/10.1016/j.jallcom.2024.173490.

31. C. V. Thompson and R. Carel, "Stress and Grain Growth in Thin Films," *Journal of the Mechanics and Physics of Solids* 44 (1996): 657–673, https://doi.org/10.1016/0022-5096(96)00022-1.

32. D. König, P. Buenconsejo, D. Grochla, S. Hamann, J. Pfetzing-Micklich, and A. Ludwig, "Thickness-Dependence of the B2-B19 Martensitic Transformation in Nanoscale Shape Memory Alloy Thin Films: Zero-Hysteresis in 75 nm Thick Ti51Ni38Cu11 Thin Films," *Acta Materialia* 60 (2012): 306–313, https://doi.org/10.1016/j.actamat.2011.09.037.

33. T. Oellers, D. König, A. Kostka, S. Xie, J. Brugger, and A. Ludwig, "Shape Memory Micro- and Nanowire Libraries for the High-Throughput Investigation of Scaling Effects," *ACS Combinatorial Science* 19 (2017): 574–584, https://doi.org/10.1021/acscombsci.7b00065.

34. F. Lambrecht, C. Lay, I. R. Aseguinolaza, V. Chernenko, and M. Kohl, "NiMnGa/Si Shape Memory Bimorph Nanoactuation," *Shape Memory and Superelasticity* 2 (2016): 347–359, https://doi.org/10.1007/s40830-016-0080-1.

35. C. Bechtold, C. Chluba, C. Zamponi, E. Quandt, and R. L. de Miranda, "Fabrication and Characterization of Freestanding NiTi Based Thin Film Materials for Shape Memory Micro-Actuator Applications," *Shape Memory and Superelasticity* 5 (2019): 327–335, https://doi.org/10.1007/s40830-019-00239-0.

36. X. Huang and A. G. Ramirez, "Effects of Film Dimension on the Phase Transformation Behavior of NiTi Thin Films," *Applied Physics Letters* 95 (2009), https://doi.org/10.1063/1.3226104.

37. A. V. Shelyakov, N. N. Sitnikov, A. P. Menushenkov, V. V. Koledov, and A. I. Irjak, "Nanostructured Thin Ribbons of a Shape Memory TiNiCu Alloy," *Thin Solid Films* 519 (2011): 5314–5317, https://doi.org/10.1016/j.tsf.2011.01.118.

38. A. V. Mashirov, A. V. Irzhak, A. V. Koshelev, et al., "Shape Memory Effect in Microsize Sample of Ni–Mn–Ga–Cu Heusler Alloy," *Physics of the Solid State* 62 (2020): 968–971, https://doi.org/10.1134/S1063783420060153.

Supporting Information

Additional supporting information can be found online in the Supporting Information section. **Supporting Fig. S1:** EDX elemental maps showing the compositional homogeneity of the 150 nm Ti-Ni-Cu thin films across the 100 mm diameter wafer, (a) Ti, (b) Ni and (c) Cu. The compositional variations are below the resolution limit of EDX. **Supporting Fig. S2:** BF-TEM analysis of the cross-section of the Ti-Ni-Cu SMA in the as-deposited state. Selected area diffraction pattern confirms the amorphous structure of the film. **Supporting Table S1:** Composition measurement of Ti-Ni-Cu SMA thin films with different thicknesses. Data compares the as-deposited state with the post-annealed for 2 h at 600°C for each thickness. **Supporting Table S2:** Results of residual stress measurements of Ti-Ni-Cu SMA thin films with different thicknesses via DHM methods on Si micro-cantilever stress chip. Data compares the as-deposited state with the post-annealed for 2 h at 600°C for each thickness.